

WETTABILITY ANALYSIS USING MICRO-CT, FESEM AND QEMSCAN, AND ITS APPLICATIONS TO DIGITAL ROCK PHYSICS

Nasiru Idowu¹, Haili Long¹, Pål-Eric Øren¹, Anna M. Carnerup², Andrew Fogden³, Igor Bondino⁴ and Lars Sundal⁵

¹ FEI Trondheim AS, Trondheim, Norway; ² FEI Australia Pty Ltd, Canberra, Australia;

³ Australian National University, Canberra, Australia; ⁴ Total E&P, Pau, France;

⁵ DEA Norge AS, Oslo, Norway

This paper was prepared for presentation at the International Symposium of the Society of Core Analysts held in St. John's Newfoundland and Labrador, Canada 16-21 August, 2015

ABSTRACT

This study presents an integrated methodology for determining the pore-scale distribution of wettability of rock samples to guide pore network modeling. Wettability was characterized by spatial registration of rock images from X-ray micro-computed tomography (MCT), Field Emission Scanning Electron Microscopy (FESEM), and Quantitative Evaluation of Minerals by SEM (QEMSCAN). The approach was applied to miniplugs of an outcrop and a reservoir sandstone, which were drained and aged in oil and underwent spontaneous and forced imbibition of brine. Tomogram acquisition after each preparation step showed that, from similarly low initial water saturation, oil recovery by spontaneous imbibition was high in the outcrop and virtually zero in the reservoir sample, while the additional recovery by forced imbibition was the opposite. These results and the pore-scale distributions of remaining oil suggest different wettabilities for each sample though their petrophysical properties (porosity and permeability) are similar.

The cleaned miniplugs were then subjected to FESEM mapping of raw cut faces to visualize local wettability alteration, and to QEMSCAN of polished faces to relate this to surface mineralogy. The established wettability information was then used to assign plausible wettability parameters to pores and throats of topologically equivalent networks. The simulated oil/water displacement results for the reservoir sandstone showed good agreement with available SCAL data.

INTRODUCTION

Optimal recovery from hydrocarbon reservoirs during waterflooding and enhanced oil recovery techniques depends largely on a good understanding of crude oil/brine/rock interactions – wettability [1]. To classify reservoir wettability either as water- or oil-wet is a gross oversimplification that can lead to unexpectedly low oil recovery and inefficient reservoir management [2, 3]. A mixed-wet state is often inferred, but without sufficient information to determine its detailed distribution. The three standard

measurement methods for quantitatively characterizing wettability of rock samples are contact angle goniometry [4], and the Amott [5] and USBM [6] tests based on spontaneous and forced imbibition/drainage. Goniometry is restricted to a prepared rock section, which often limits measurement precision. Amott and USBM tests only yield an averaged wettability measure of a core sample, and the former is relatively insensitive near neutral wettability. Complementary wettability information can be obtained from, e.g. spontaneous imbibition rates, relative permeability, calorimetry, flotation of crushed rock or microscopy of model substrates, although the results are often less quantitative or less directly relevant. Nuclear magnetic resonance (NMR) methods have also been used to provide quantitative wettability indices [7, 8].

Advanced, high-resolution imaging techniques such as MCT and FESEM have recently been used to determine the pore-scale distribution of oil in rock plugs before, during or after waterflooding and to visualize the asphaltene films remaining on cleaned rock surfaces due to local wettability alteration [9-13]. To date, establishment of quantitative links between these imaging studies and connections to prediction of residuals are limited. Andrew *et al.* [14] recently presented a method for contact angle measurement from MCT of a supercritical CO₂-brine system in a Ketton limestone. However, this rock has simple mineralogy, comprising 99.1% calcite and 0.9% quartz [14].

In this study, we establish the wettability of reservoir and outcrop sandstone samples by integrating imaging results from MCT, FESEM and QEMSCAN. Secondly, we use this information to assign plausible wettability parameters to pores and throats of topologically equivalent pore networks extracted from the segmented pore space. Finally, we simulate oil/water displacements with a quasi-static pore network model and compare the results with available experimental data.

MATERIALS AND METHODS

Two sandstone samples were used in this study. MCT (by HeliScan) of the received core plugs (25 mm) showed that the outcrop Sample 1 was fairly homogenous while the reservoir Sample 2 was highly heterogeneous with several laminations. Locations within these low resolution tomograms were chosen for subsampling of two miniplugs of 6 mm × 15 mm and 9 mm × 10 mm from each, using a manually-fed drill press. The miniplugs were cleaned by hot Soxhlet extraction in toluene, methanol and chloroform/methanol azeotrope, and then dried. Mercury injection capillary pressure (MICP) measurements were performed on the 9 mm diameter miniplugs while the 6 mm diameter miniplugs were used in the remainder of the study. The measured petrophysical properties are summarized in Table 1.

Tomograms of the pair of 6 mm miniplugs were acquired (at 3.7 or 3.9 μm/voxel resolution for Samples 1 and 2, respectively) in a series of five prepared states, starting with their cleaned, dry state. Each miniplug was then infiltrated, under vacuum followed by high isostatic pressure, with brine comprising 5 g/l CaCl₂, doped with 1.5 M NaI, after which this brine-saturated state was scanned. Primary drainage was then carried out by

centrifugation in the supplied crude oils to a maximum capillary pressure of 500 kPa for a minimum of 12 h, followed by 14 days of ageing at 60°C or 83°C for Samples 1 and 2, respectively. The third tomogram was acquired in this state of established initial water saturation and wettability alteration. The miniplug was then immersed in the same brine and temperature as mentioned above for 7 days of spontaneous imbibition, followed by re-scanning. Forced imbibition was then performed by centrifugation in this brine to a maximum pressure of 17.5 or 14.0 kPa for Samples 1 and 2, respectively, for at least 18 h, after which this fifth state was imaged.

Table 1. Measured petrophysical properties of the two sandstone samples.

Sample No.	Porosity (%)	Kabs (mD)
1 (outcrop)	22.5	524
2 (reservoir)	22.7	853

Each miniplug was then cleaned of its remaining oil using decalin and heptane, followed by centrifugation in the undoped brine, prior to being cut in half crosswise using a Struers saw with water-based coolant. After removal of salt by soaking in methanol, the bottom half was re-scanned and then imaged by FESEM (Helios 600 NanoLab, FEI) using a secondary electron detector. Its raw cut face was first mapped at 0.59 $\mu\text{m}/\text{pixel}$, followed by acquisition of higher magnification micrographs at selected locations to resolve the asphaltene footprint (or lack of) on pore walls. The top half of the miniplug was resin embedded for preparation of a polished face for analysis by SEM (Quanta 650 FEG, FEI) using a backscattered electron detector for imaging and Energy-dispersive X-ray spectroscopy for mineral identification, automated by MAPS software and QEMSCAN.

RESULTS

MCT Imaging and Analysis

For each of the two 6 mm miniplugs, their series of five tomograms were post-processed by Mango software for 1) spatial registration to within one voxel, 2) correction of beam hardening artifacts, 3) cylindrical masking of the damaged periphery, and 4) rescaling of attenuation. The processed tomograms and their differences were then segmented using converging active contours algorithms to identify solid grains, pores and sub-resolution microporosity. The oil and brine occupancy of each voxel of these latter two categories at the end of primary drainage and ageing (PD), and spontaneous (SI) and forced imbibition (FI) was identified. For the segmented porosity and water saturation of Samples 1 and 2, Table 2 lists their tomogram averages, Figure 1 plots their (radially-averaged) longitudinal profiles, and Figure 2 shows a representative cross-sectional slice, in which rock, oil and water correspond to grayscales, red and blue, respectively. The top (≈ 5 mm) and more porous part of the Sample 2 miniplug broke after PD and the remaining piece was used for aging, SI and FI. The lower segmented porosity in Table 2 compared to Table 1 and the shorter profile length in Figure 1 are due to this breakage.

Table 2. Average segmented porosity and water saturation from MCT of 6 mm diameter miniplugs.

Sample No.	Porosity (%)	Swi_PD (%PV)	Sw_SI (%PV)	Sw_FI (%PV)
1	20.7	3.0	59.3	62.9
2	17.4	3.2	4.5	34.1

The two miniplugs have similar measured petrophysical properties (Table 1) and comparable S_{wi} after primary drainage and aging (Table 2, which may be underestimated due to limitations in resolving brine thin films). However, the corresponding profiles in Figure 1 show that the outcrop Sample 1 is homogeneous while the reservoir Sample 2 is heterogeneous with tighter and more open laminations. The two miniplugs also exhibit very different imbibition response. Sample 1 shows very strong spontaneous imbibition, while Sample 2 has almost none, aside from the rise near the ends which is common to both. Additional recovery by forced imbibition is limited for Sample 1, but substantial for Sample 2, and with heterogeneities partly mirroring those of its porosity profile. The computed Amott water indices (I_w) from segmentation of the oil and water phases in Samples 1 and 2 are in the ranges 0.60-0.94 and 0.01-0.04, respectively.

Figure 2a shows that the irreducible water of the 6 mm Sample 1 miniplug resides as expected in the tightest locations and in the relatively rare clay-aggregate particles. Given the predominance of grain-lining clays, much of the water may remain connected, in spite of its overall low saturation. By contrast, the irreducible water of the 6 mm Sample 2 miniplug in Figure 2d appears less connected, due to its smoother grains with less clay lining and the occlusion of tighter pores by a slightly lower-attenuating (darker) mineral cement. However, it should be borne in mind that S_{wi} of this slice is only 1.5 %, as it comes from the lowest-saturation dip of the blue curve (Swi_PD profile) in Figure 1b.

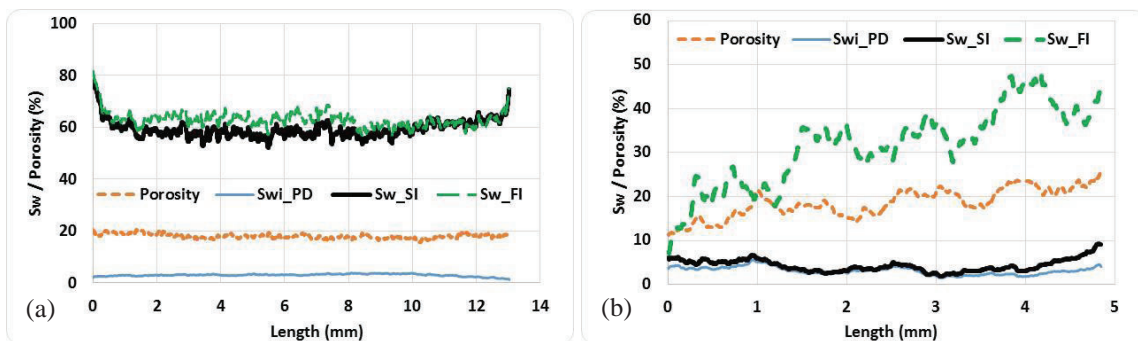


Figure 1. Longitudinal profiles of porosity (% bulk volume) and S_w (% PV) after primary drainage, spontaneous and forced imbibition, for the miniplugs of (a) Sample 1 and (b) Sample 2.

The substantial spontaneous imbibition into Sample 1 in Figure 2b recovers virtually all oil from smaller pores and near grain surfaces to leave large blobs in pore bodies (e.g. highlighted with green boxes), presumably due to snap-off in throats. Virtually no further change is seen on forced imbibition in Figure 2c. Conversely, the change in Sample 2 from Figure 2d to 2e due to spontaneous imbibition is almost imperceptible, while subsequent forced imbibition in Figure 2f results in complete recovery of oil from many

of the larger pores (e.g. highlighted with yellow circles). The remaining oil generally occupies narrower pores closest to grain surfaces, and retains higher connectivity than for Sample 1. Larger uninvaded clusters, e.g. at upper left in Figure 2f, may be due to the miniplug heterogeneity. The computed I_w and the pore-scale remaining oil distributions suggest that Sample 1 is water-wet while Sample 2 is oil-wet.

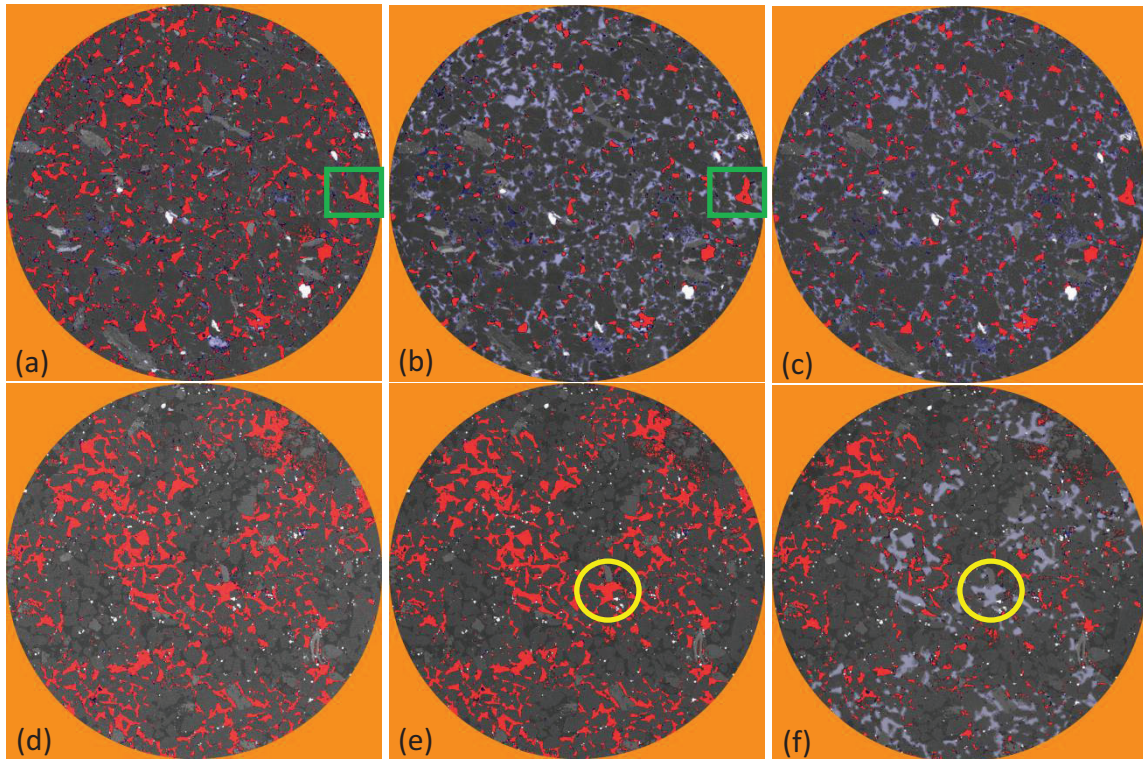


Figure 2. Registered tomogram slices of (a-c) Sample 1 and (d-f) Sample 2, showing oil (red) and brine (blue) distribution after (a, d) primary drainage, (b, e) spontaneous and (c, f) forced imbibition.

QEMSCAN

Figure 3 shows registered automated maps from backscattered electron SEM imaging and QEMSCAN mineral identification on a polished embedded section within the upper half of the miniplugs of Samples 1 and 2, which do not coincide with the tomogram slices in Figure 2. From Figure 3b, almost 40% of all grains in Sample 1 comprise Na plagioclase, although these are indistinguishable from the quartz grains in Figures 2a-c and 3a owing to their similar X-ray attenuation and electron density, respectively. Feldspar corresponds to the slightly brighter grains in MCT, which are relatively rare. The prevalent flaky particles are mainly muscovite with occasional biotite, and particles and seams of detrital chlorite are fairly common. These clays are the brighter mineral features in Figures 2a-c and 3a, while the brightest grains correspond to the densest trace minerals. Illite and biotite in the form of grain-lining plates are under-represented due to resolution limitations of both QEMSCAN (2.4 $\mu\text{m}/\text{pixel}$) and MCT. Figure 3d shows that Sample 2 is also dominated by quartz and Na plagioclase. The latter is the cement-like phase in

Figures 2c-f and 3c of slightly lower X-ray attenuation and electron density, respectively, than the surrounding quartz grains. Feldspar is more prevalent than in Sample 1, while clays are less common, although their presence as grain linings may again be underestimated. Figure 3c shows quite substantial damage to Sample 2 during resin stub preparation, while Sample 1 in Figure 3a remained intact.

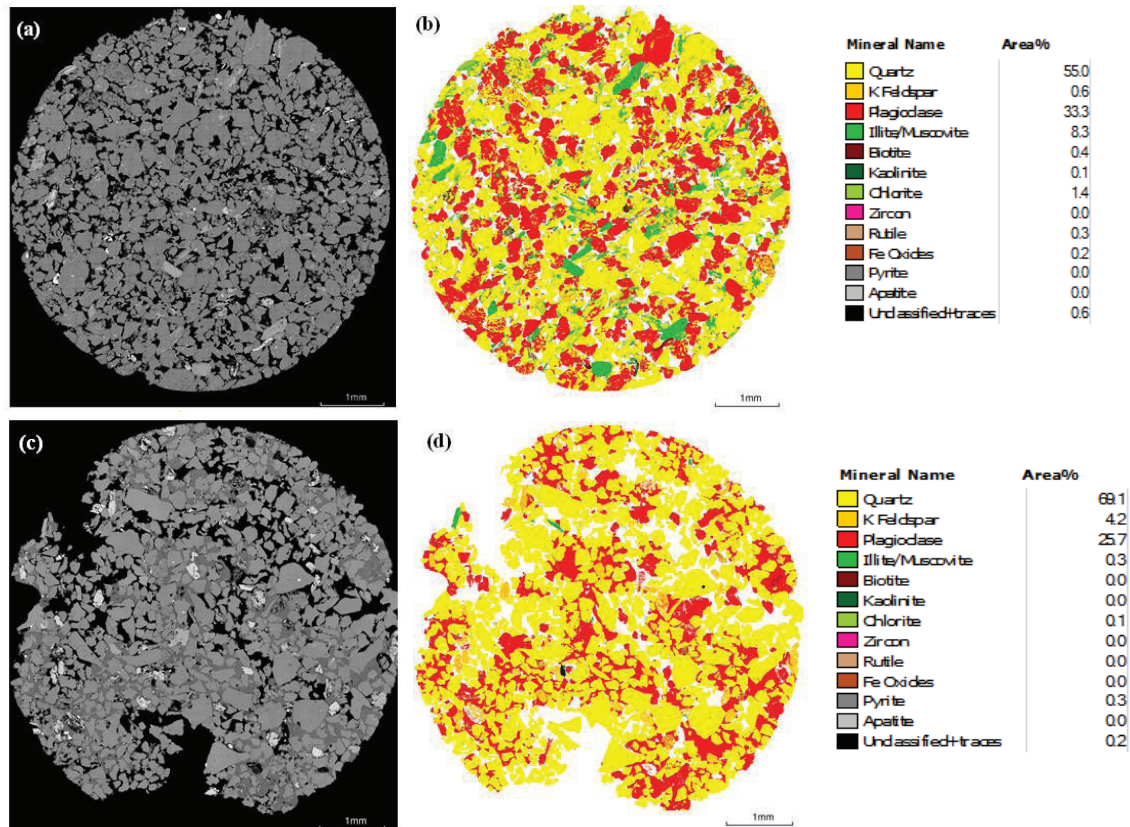


Figure 3. Registered maps of a polished cross-section of the 6 mm miniplugs of (a-b) Sample 1 and (c-d) Sample 2, by (a, c) backscattered electron SEM mapping and (b, d) QEMSCAN mineral mapping.

FESEM Imaging

The FESEM map of a rectangular subarea of the raw cut face of the cleaned, dry miniplug of Samples 1 and 2 is shown in Figures 4a and 4c, respectively. This 2D map was registered into the 3D tomogram series via the intermediate step of registering the tomogram of the cut (half-) miniplug to its uncut counterpart [12]. The uppermost voxel at each position on the cut face was identified by segmentation to yield its height map. The FESEM map was then 2D-2D registered to the vertical projection of these uppermost voxels onto a flat plane. The voxels corresponding to this same height map in the original miniplug tomogram, and all others in the series, were then similarly projected. Smoothing of the grain-hugging height map was also performed so that it spans the pore bodies. Figures 4b and 4d show the resulting registered projection of the tomograms after spontaneous and forced imbibition of Samples 1 and 2, respectively. This procedure served to identify subregions in the FESEM map which were free from debris and

plucking damage and where the oil's pore occupancy and grain contact displayed interesting imbibition history, for inspection by higher-resolution FESEM imaging.

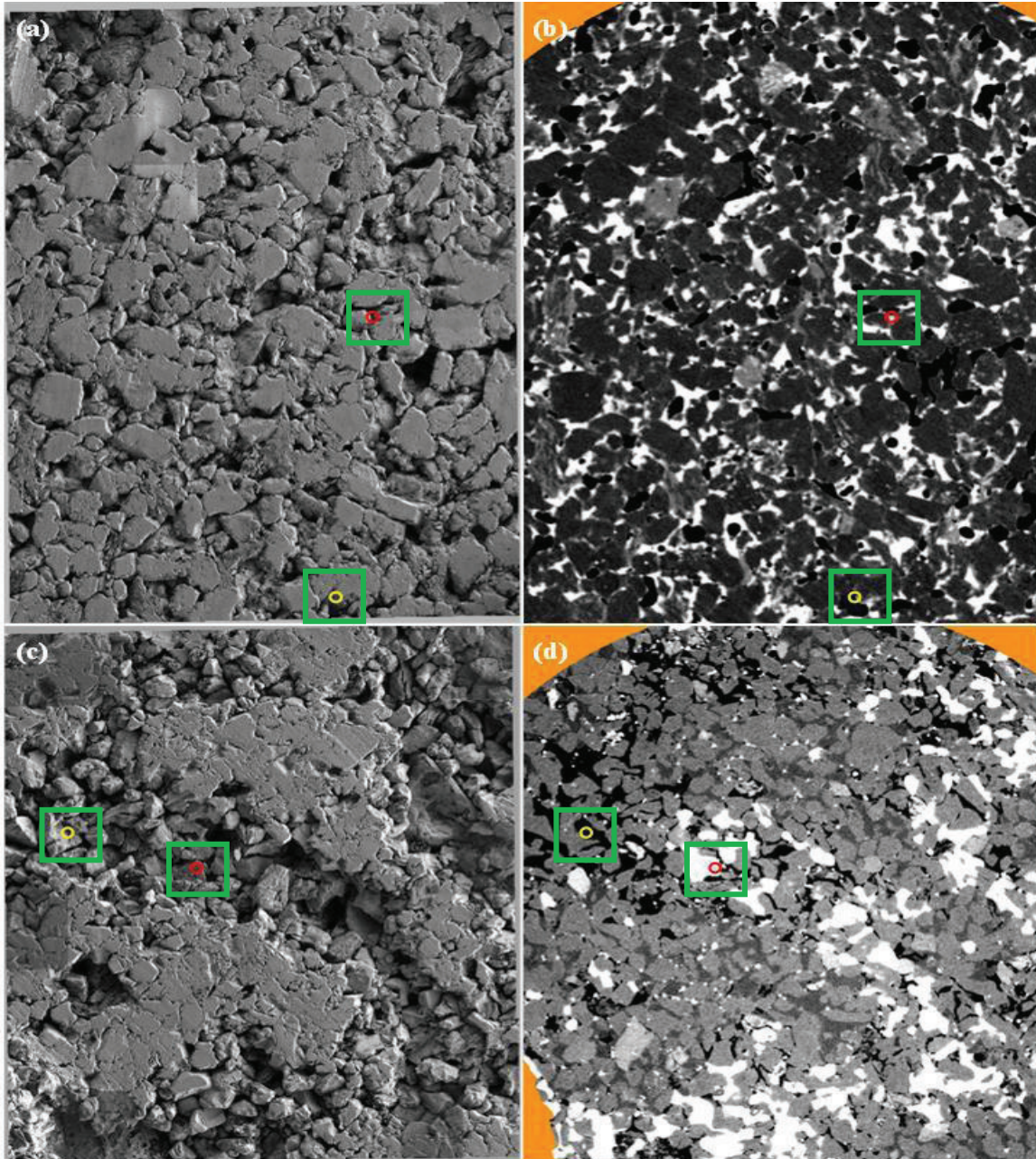


Figure 4. Low resolution FESEM mosaic of cut face of (a) Sample 1 (3.3 mm x 4.5 mm) and (c) Sample 2 (3.8 mm x 4.5 mm), and registered smoothed tomogram projection of (b) Sample 1 after spontaneous imbibition and (d) Sample 2 after forced imbibition, with brine in white and oil in black.

The micrographs in Figure 5 are from the center of the circles marked in Figure 4, all of which were oil-filled after primary drainage. Within the yellow circle in Figure 4b of

Sample 1, the oil blob trapped in this pore body after spontaneous imbibition is locally anchored to a grain. The corresponding close-up of a quartz overgrowth of this grain in Figure 5a shows a light scattering of asphaltene nanoparticles, suggestive of a weakly water-wet surface and possibly accounting for the blob attachment there. Moreover, none of the multitude of high resolution FESEM images acquired of Sample 1 showed substantially greater asphaltene coverage than this, implying that the majority of its surfaces are weakly to strongly water-wet. Figure 5a also exhibits another common feature of Sample 1, namely debris in the form of very fine clay platelets on oil-exposed regions. Within the red circle in Figure 4b, spontaneous imbibition detached the oil from an illite-coated grain. The corresponding close-up in Figure 5b, and others in this neighborhood, displays no asphaltene deposit, in line with the expectation that grain-lining clays aid retention of water and water-wetness to cause oil snap-off.

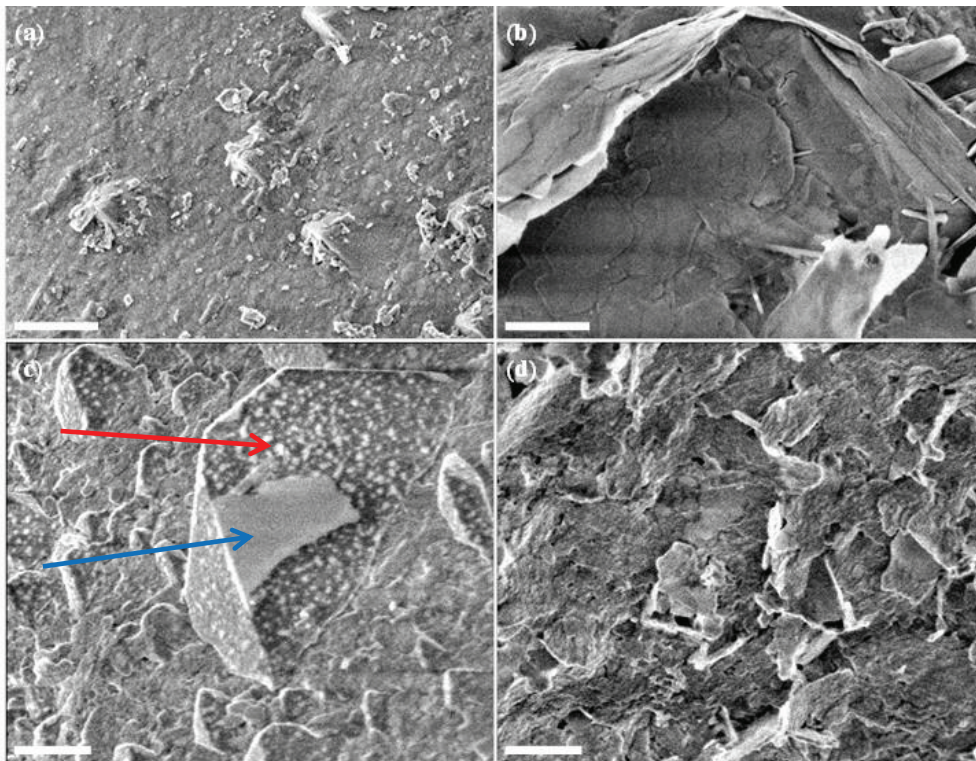


Figure 5. High resolution FESEM images, all with 0.5 μm scale bars, of raw cut face of Sample 1 at the location of the (a) yellow and (b) red circle in Figure 4a-b, or of Sample 2 at the location of the (c) yellow and (d) red circle in Figure 4c-d.

Within the yellow circle in Figure 4d of Sample 2, the pore remains oil-filled after forced imbibition. The close-up in Figure 5c of a grain with quartz overgrowths bounding this pore is representative of the much heavier deposits of asphaltene than on Sample 1. Film coverage is almost complete, aside from the so-called dalmation pattern of bright perforations from brine nano-droplets trapped under the film during primary drainage and aging (arrowed). Other occasional bare patches (also arrowed) may be caused by fines detachment by moving contact lines during cleaning.

Within the red circle in Figure 4d, forced imbibition removes oil from a grain that is partly smooth and partly lined by clay, a close-up from the latter of which is given in Figure 5d. In contrast to Sample 1, the clay linings of Sample 2, in this and all other inspected regions, appear completely covered by asphaltene. This is again consistent with the oil-wetness inferred from MCT, and suggests that local retention of oil, such as in the vicinity of Figure 5c, is due to reasons other than mineralogy. QEMSCAN in Figures 3b and 3d showed that Samples 1 and 2 are both dominated by quartz and plagioclase, lined by illite to varying extents. Further, the same brines were used for both samples and were drained to similar S_{wi} values. Thus the strong wettability differences observed in MCT and FESEM are most likely due to the different crude oils, with density of 835 and 900 kg/m^3 , used for Samples 1 and 2, respectively.

COMPARISON OF SIMULATED RESULTS WITH EXPERIMENTAL DATA FOR SAMPLE 2

Topologically equivalent pore networks [15] were extracted from the segmented pore space of the miniplug dry tomogram. To establish whether or not the pore networks are representative, oil/water primary drainage displacement was simulated using a quasi-static pore network model [16]. The resulting oil/water $P_c - S_w$ curves were scaled into mercury/air $P_c - S_w$ curves using interfacial tensions and contact angles [17]. Figure 6a compares the measured MICP data on the 9 mm diameter miniplug with the simulated data on the 6 mm miniplug, and Figure 6b shows the oil/water primary drainage relative permeability curves. The measured and simulated MICP are in good agreement within the limits of image resolution, suggesting that the pore networks are representative.

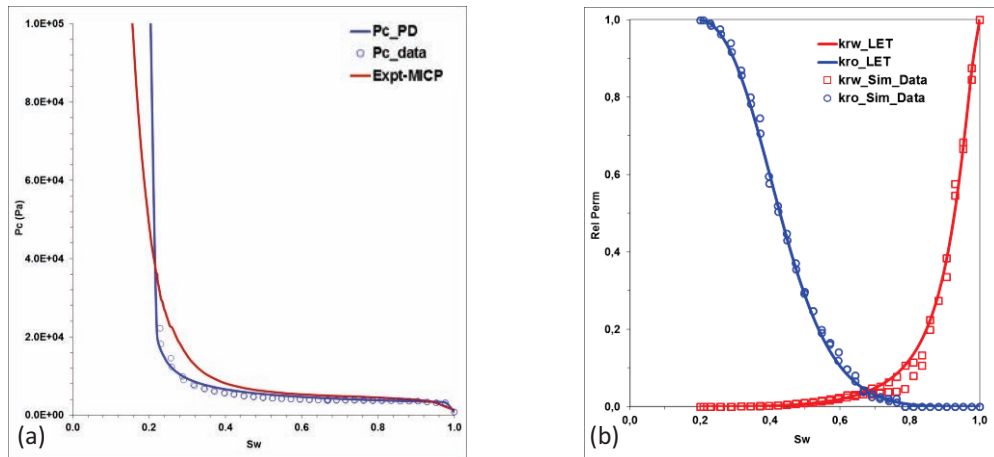


Figure 6. (a) Comparisons of simulated (Sim) and experimental (Expt) MICP data, and (b) primary drainage oil/water relative permeability curves for Sample 2. The blue circles and red squares are the simulated data points fitted to the corresponding lines.

Based on the wettability results presented above, we then assigned plausible wettability input parameters to pore network elements of Sample 2 for simulation of imbibition processes. In particular, the fraction of pores contacted by oil that changed wettability

from water- to oil-wet was 1.0, and the minimum and maximum advancing contact angle for oil-wet pores was 100° and 150° , respectively. Simulations of oil/water displacements were then performed for comparison with available data from special core analysis.

The experiments used a composite core of four plugs, from the same formation as Sample 2, with a porosity of 24% and effective oil permeability of 854 mD at S_{wi} of 0.251. The simulation was on pore networks extracted from the Sample 2 miniplug with a porosity of 17.4%, computed grid permeability of 699 mD and simulated S_{wi} of 0.20. Figure 7a compares the porous plate primary drainage (PD) and spontaneous imbibition (SI) capillary pressure data, using dead crude oil on the four plugs, with simulated data. Forced imbibition (FI) measurement carried out on one of the four plugs gave one additional data point at -60 kPa as shown in Figure 7b. The volume of water spontaneously imbibed and the calculated I_w from the porous plate experiments, MCT imaging and simulations are summarized in Table 3, with good quantitative agreement between the data.

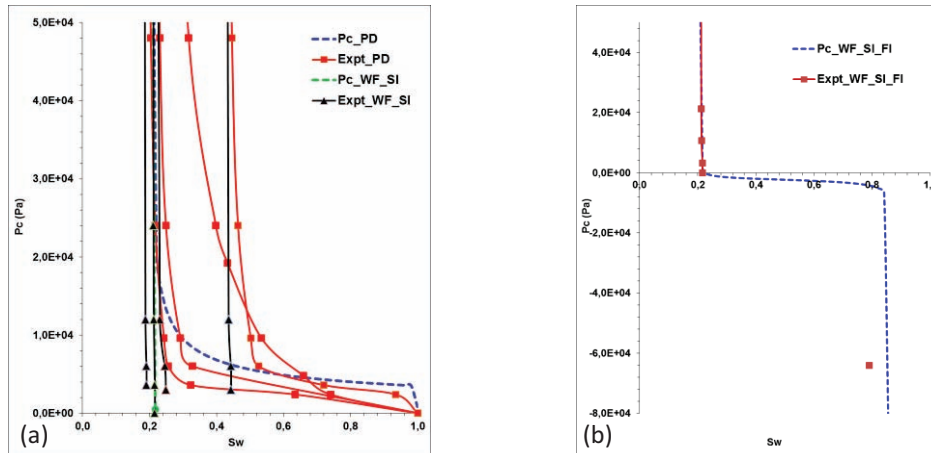


Figure 7. Comparisons of simulated (dashed line) with porous plate experimental capillary pressure data (solid line) for Sample 2. (a) Primary drainage (PD) and spontaneous imbibition (SI), and (b) SI and forced imbibition (FI).

Table 3. Volume of brine spontaneously imbibed and calculated Amott water indices.

	Volume of brine spontaneously imbibed (% PV)	Calculated I_w
Porous plate experiment	1.0-5.0	0.014
MCT imaging	1.3	0.010-0.040
Simulation	1.2	0.018

To eliminate the influence of the different S_{wi} values, the imbibition relative permeability data were normalized. The composite core measured data were history-matched with a Sendra core flooding simulator to produce the experimental LET [18] curve fit. Figure 8 compares the normalized simulated relative permeability results to those from experiment. Considering the heterogeneity of Sample 2 and the difference in scale

between the core experiment and the miniplug simulation, the measured relative permeability compares qualitatively well with the simulation.

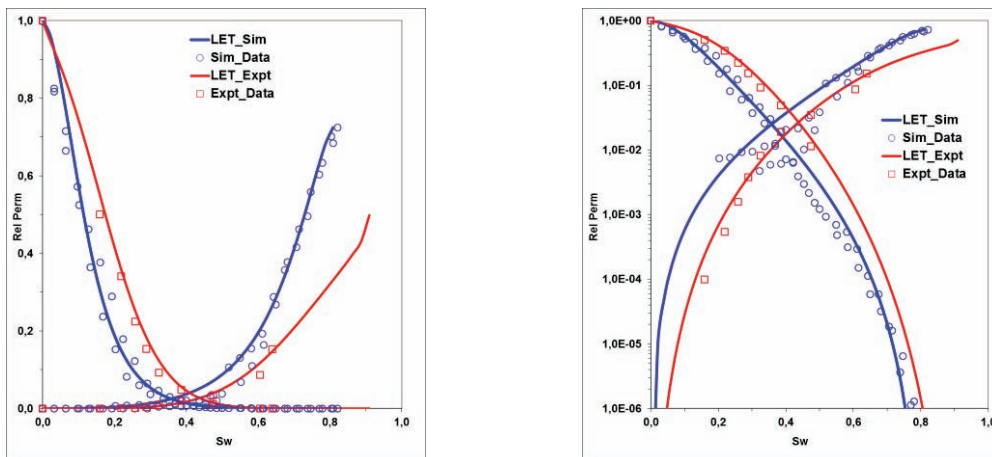


Figure 8. Comparisons of simulated (Sim) and experimental (Expt) oil/water relative permeability curves for Sample 2. The blue circles and the red squares are the simulated data points fitted to the corresponding lines.

CONCLUSIONS

The pore-scale distribution of water in the initial state, and spontaneously and forcibly imbibed, from MCT imaging and registration can provide useful information on the pore-scale distribution of wettability. Integration of FESEM images at raw surfaces provides complementary insight at higher resolution, and combination with QEMSCAN of embedded sections can shed light on mineral-specific wettability. Although the two samples studied proved to be fairly uniformly water-wet and oil-wet, this imaging framework can greatly benefit the interpretation of more complex mixed-wet samples. Network modelling of multiphase transport properties incorporating this wettability identification showed good quantitative/qualitative agreement with experimental data, despite the difference in scale.

ACKNOWLEDGMENTS

The authors acknowledge FEI Trondheim AS for granting permission to publish this paper, which is partly funded by DEA Norge AS and Norwegian Research Council through PETROMAKS Project Number: 208772/E30, titled: “Physically based three-phase relative permeability relations”. We also thank STATOIL, TOTAL and DEA for sharing their samples and data with us. Jill Middleton (ANU) is thanked for assistance with FESEM-MCT registration.

REFERENCES

1. Anderson, W.G., “Wettability Literature Survey – Part 1: Rock/Oil/Brine Interactions and the Effects of Core Handling on Wettability”, *J. Pet. Tech.* (1986), **38**: 1125-1144.

2. Morrow, N.R., “Wettability and its Effects on Oil Recovery”, *J. Pet. Tech.* (1990), **42**: 1476-1484.
3. Abdallah, W., Buckley, J.S., Carnegie, A., *et al.*, “Fundamentals of Wettability”, *Oilfield Review*. Summer 2007: 44-61.
4. Anderson, W.G., “Wettability Literature Survey – Part 2: Wettability Measurement”, *J. Pet. Tech.* (1986), **38**: 1246-1262.
5. Amott, E., “Observations Relating to the Wettability of Porous Rock”, *Trans. AIME*, (1959), **216**: 156-162.
6. Donaldson, E.C., Thomas, R.D. and Lorenz, P.B., “Wettability Determination and its Effect on Recovery Efficiency”, *SPE Journal*, (1969) **9**: 13-20.
7. Freedman, R., Heaton, N., Flaum, M., *et al.*, “Wettability, Saturation, and Viscosity From NMR Measurements” *SPE Journal*, (2003) **8**: 317-327.
8. Looyestijn, W. J., and Hofman, J., “Wettability Index Determination from NMR Logs”, SPE-93624-MS (2005). doi:10.2118/93624-MS.
9. Kumar, M., Fogden, A. and Senden, T., “Investigation of Pore-Scale Mixed Wettability”, *SPE Journal*, (2012) **17**: 20-30.
10. Fogden, A., Kumar, M., Morrow, N.R., *et al.*, “Mobilization of fine particles during flooding of sandstones and possible relations to enhanced oil recovery”, *Energy Fuels*, (2011) **25**: 1605-1616.
11. Marathe, R., Turner, M.L., and Fogden, A., “Pore scale distribution of crude oil wettability in carbonate rocks”, *Energy Fuels* (2012), **26**: 6268-6281.
12. Dodd, N., Marathe, R., Middleton, J., *et al.*, “Pore-Scale Imaging of Oil and Wettability in Native-State, Mixed-Wet Reservoir Carbonates”, Paper IPTC 17696, (2014).
13. Lebedeva, E.V. and Fogden, A., “Micro-CT and wettability analysis of oil recovery from sandpacks and the effect of waterflood salinity and kaolinite”, *Energy Fuels*, (2011), **25**: 5683-5694.
14. Andrew, M., Bijeljic, B., and Blunt, M.J., “Pore-scale Contact Angle Measurements at Reservoir Conditions Using X-ray Microtomography”, *Advances in Water Resources*. (2014), **68**: 24-31.
15. Bakke, S., and P.E. Øren, “3-D pore-scale modelling of sandstones and flow simulations in the pore networks,” *SPE Journal*, (1997), **2**, 136-149.
16. Øren, P.E., S. Bakke, and O.J. Arntzen, “Extending Predictive Capabilities to Network Models”, *SPE Journal*, (1998), **3**, 324-336.
17. Idowu, N., Nardi, C., Long, H., *et al.*, “Improving Digital Rock Physics Predictive Potential for Relative Permeabilities From Equivalent Pore Networks”, Paper SCA2013-17, Proceedings of the 2013 SCA Symposium, Napa Valley, California, USA, 16 -19 September , 2013.
18. Lomeland, F., Ebeltoft, E., and Thomas, W. H., “A new versatile relative permeability correlation”, Paper SCA2005-32. Proceedings of the 2005 SCA Symposium, Toronto, Canada, 21-25 August, 2005.